







Breaking Location of Internal Solitary Waves Over a Sloping Seabed

Davide Cavaliere^{1,2} , Giovanni la Forgia^{1,3} , Claudia Adduce^{1,3} , Werner Alpers⁴ , Eleonora Martorelli⁵ , Federico Falcini¹ 

¹Institute of Marine Sciences National Research Council, Rome, Italy, ²Department of Basic and Applied Sciences for Engineering, Sapienza University of Rome, Rome, Italy, ³Department of Civil Engineering, Roma Tre University, Rome, Italy, ⁴Institute of Oceanography University of Hamburg, Hamburg, Germany, ⁵Institute of Environmental Geology and Geoengineering National Research Council, Rome, Italy

Key Points:

- A simple analytical model, validated by laboratory experiments, predicts the internal solitary waves (ISWs) breaking location for real-field stratification conditions
- ISWs fronts are revealed by Synthetic Aperture Radar images, and are observed to refract, interacting orthogonally with the frontal slope
- Location of ISWs verticalization suggests a relation between the waves breaking and the presence of morpho-sedimentary features

Correspondence to:

G. La. Forgia,
giovanni.laforgia@uniroma3.it

Citation:

Cavaliere, D., la Forgia, G., Adduce, C., Alpers, W., Martorelli, E., & Falcini, F. (2021). Breaking location of internal solitary waves over a sloping seabed. *Journal of Geophysical Research: Oceans*, 126, e2020JC016669. <https://doi.org/10.1029/2020JC016669>

Received 5 AUG 2020
Accepted 28 NOV 2020
Corrected 24 MAR 2021

This article was corrected on 24 MAR 2021. See the end of the full text for details.

Abstract We present a semi-analytical model for predicting the breaking location of internal solitary waves (ISWs) over a sloping seabed. Our conceptual model is based on laboratory experiments, performed in a wave tank, that reproduce the ISW breaking mechanisms and show how the steepening of the trailing edge leads to verticalization of the wave profile during the shoaling phase. We derive the location of ISWs breaking, that is, the wave verticalization point, through two-layer, interfacial theoretical models and conservation of wave mass. We apply our model to the case of tidally forced ISWs that are generated in the Strait of Messina (Central Mediterranean Sea), where northward traveling ISWs are expected to refract and break over the frontal slope of Capo Vaticano. Our application is then assessed through numerical investigations, which allow to consider realistic field conditions in terms of water column stratification and geometrical setting. Our results, and the expected ISW-induced bed shear stress, suggest a link between the predicted breaking locations and the occurrence of sediment resuspension over that specific portion of the slope.

Plain Language Summary Internal solitary waves (ISWs), generated by tidal effects, represent one of the most investigated phenomena within the Messina Strait (Mediterranean Sea). In the Tyrrhenian Sea they propagate northward, toward the frontal steep slope of Capo Vaticano (Calabria, Italy), where their refraction and breaking are expected to occur. Since direct measurements of breaking are difficult to set up; this is indirectly confirmed by both Synthetic Aperture Radar images and previous in situ observations. In our investigation, we develop a semi-analytical model that predicts breaking location of ISWs over the sloping seabed. Morpho-sedimentary features are present south of the Capo Vaticano frontal slope, where ISWs are expected to break. Our conceptual model is built on experimental results that are obtained from laboratory investigation. We analyze the experimental wave profiles and assess the location of ISWs breaking through two-layer interfacial models. By using a continuously stratified theoretical model, we assess the validity of the two-layer models under realistic conditions of water column stratification and domain extension. This confirms the applicability of our theoretical model for predicting the ISWs breaking location in a more realistic scenario.

1. Introduction

Internal solitary waves (ISWs) consist of hump-shaped large undulations of the pycnocline with a permanent form, resulting from a balance between nonlinearity, which tends to steepen it, and dispersion, which tends to flatten it (Grimshaw et al., 2010; Helfrich & Melville, 2006; Sutherland et al., 2013). ISWs are mostly generated by the interaction between tidal flows and bottom topographic features, such as underwater sills and the continental shelf-slope region (Helfrich & Melville, 2006; Osborne & Burch, 1980). Packets of shoreward-propagating ISWs, separated by tidal periods, are a ubiquitous feature of the coastal oceans (Dwi Susanto et al., 2005; Helfrich & Melville, 2006; Massel, 2015).

One of the most popular “hot spots” for the observation of large amplitude ISWs is the Strait of Messina (Alpers & Salusti, 1983; Artale et al., 1990; Brandt et al., 1999), that is, a narrow channel that separates Sicily from the Italian peninsula and connects the Tyrrhenian Sea in the north and the Ionian Sea in the south (Figure 1a). The center of the Strait is about 80 m deep; the sea bottom reaches 1,300 m depth toward the

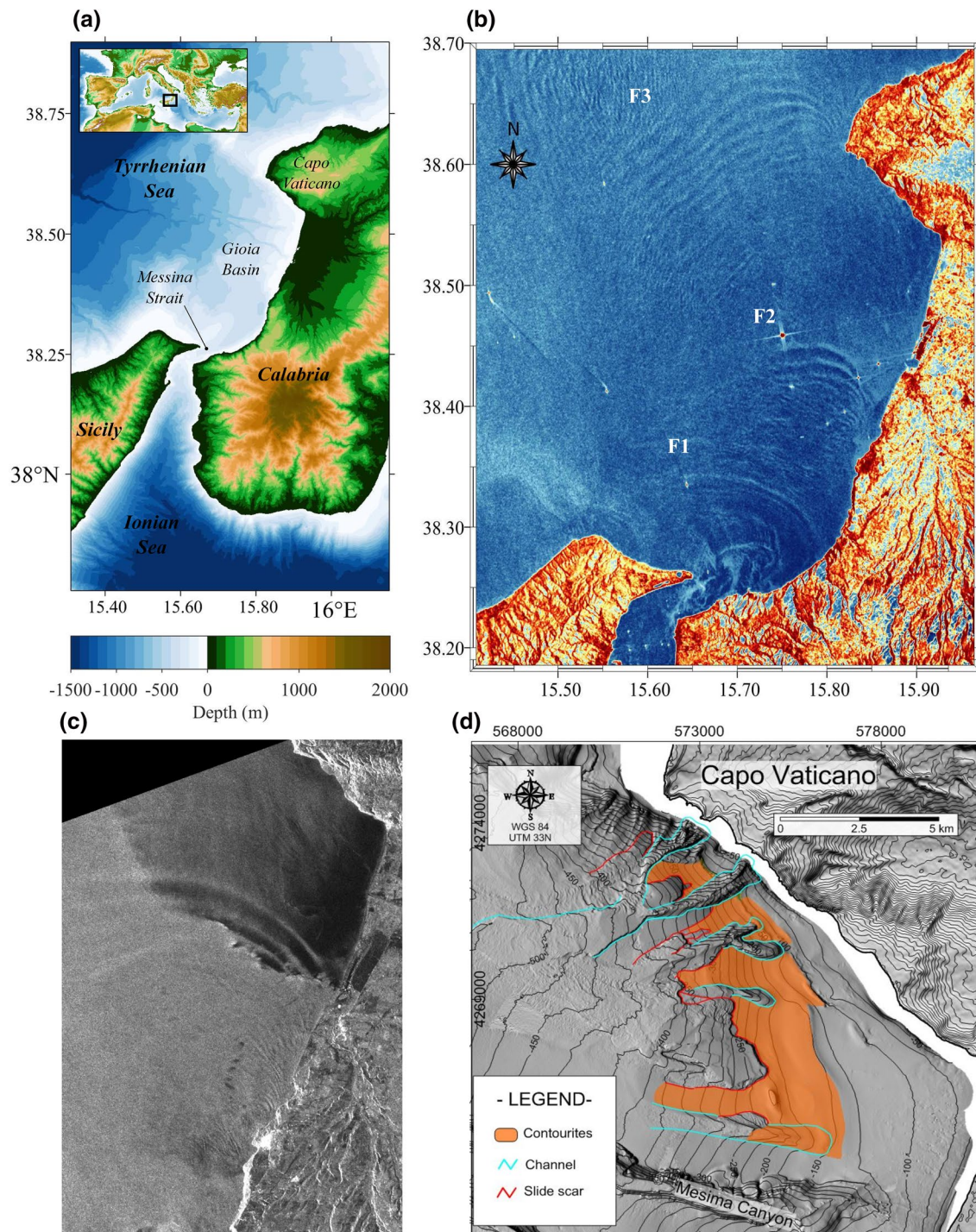


Figure 1. (a) Area of interest. (b) Sentinel 1B SAR false color image showing ISW packets propagating northward from the Messina Strait toward Capo Vaticano promontory on May 14, 2018. Three different ISW packets (i.e., F1, F2, F3) are observed, each produced at the sill region at approximately every 12 h. ISWs deflect due to a topographic constraint on the left (see F1 and F2 in (b)). Refractive phenomena also occur along the Calabrian coastline, on the right. (c) Seasat SAR image, September 15, 1978, showing the dark gray area southward of Capo Vaticano described by Marullo and Santoleri (1986). (d) Morpho-sedimentary features southward of Capo Vaticano promontory; the presence of contourites, channels, and slide scars is highlighted in orange, blue, and red, respectively. ISWs, internal solitary waves; SAR, Synthetic Aperture Radar.

Ionian Sea and 300–600 m depth at the Tyrrhenian side, that is, along the Gioia Basin, where it remains almost flat till the frontal slope of Capo Vaticano (Figure 1a).

The sill of the Strait constitutes a submarine barrier for the water flowing through the channel. In particular, it represents an amphidromic point for the semidiurnal tides of the two adjacent sub-basins (Alpers & Salusti, 1983; Brandt et al., 1999; Sapia & Salusti, 1987). During the southward tidal flow, the Tyrrhenian Surface Water (TSW) spills into the Ionian Sea; vice versa, during the northward tidal flow the denser Intermediate Levantine Water (LIW), overflowing the sill, spreads under the lighter TSW. The phase opposition of these tides generates very strong tidal currents (up to 3 m/s) at the sill region (Longhitano, 2018; Vercelli, 1925).

These tidal effects, along with the presence of the two different water masses, give rise to nonlinear ISWs of depression at the interface between LIW and TSW. These solitons propagate at about 1 m/s (Alpers et al., 2008) from the Strait toward the northern and southern mouth of the Strait, alternately (approximately with a 6-h period). ISWs off the Strait were frequently observed by both in situ (Brandt et al., 1999; Sapia & Salusti, 1987) and remote sensing measurements (Alpers & Salusti, 1983; Artale et al., 1990). Sea surface manifestations of internal waves can be detected, indeed, from Synthetic Aperture Radar (SAR) images (Alpers, 1985): they appear as brighter and darker alternate strips on the image, whether the surface waves associated to ISWs propagate in convergent or divergent surface flow zones (see Figure 1b). Evidence of ISWs is also inferred from their ability in reshaping the seafloor, giving rise to migrating bedforms (Droghei et al., 2016; La Forgia et al., 2019), and sediment resuspension (La Forgia, Tokyay, et al., 2020; Martorelli et al., 2021).

Propagating northward, nonlinear internal waves are expected to refract and break when approaching the Capo Vaticano frontal slope. Despite the absence of real-field measurements, this is revealed by indirect observations (Marullo & Santoleri, 1986): (1) the presence of a thermal front of colder water on the sea surface due to mixing processes induced by breaking; (2) SAR images show a dark gray area widespread 10 km southward of Capo Vaticano (see Figure 1c), associated with the presence of biofilms likely produced by plankton that mark deep water spun up by mixing; and (3) the presence of warm and salty water ($T \sim 14^\circ\text{C}$; $S \sim 37.8\text{--}38.6$ psu) in this zone, which indicates mixing between LIW and TSW.

Interestingly, the area southward of Capo Vaticano is characterized by a very narrow shelf and a steep continental slope, where morpho-sedimentary features, such as canyons, channels, landslides, and contourite drifts (i.e., sediments deposited and/or reworked by the persistent action of bottom currents along isobaths) determine a complex seabed morphology (Martorelli et al., 2016) (see Figure 1d). In particular, several slide events affect the elongated (i.e., distributed along the isobaths) sedimentary drifts in the upper continental slope, giving rise to the Capo Vaticano slide complex. This is composed of several intersecting slide scars and overlapping deposits and display a large spatial coverage between 200 and 500 m depth (Martorelli et al., 2016). In this particular area of the slope, the presence of such a large variety of morpho-bathymetric structures suggests the occurrence of near-bed, high-energetic events, likely induced also by the presence of ISWs, able to give rise to seafloor reshaping.

Although ISWs breaking over the frontal slope of Capo Vaticano have been largely and reasonably hypothesized from the indirect observations we listed above, there is still no direct observation as well as mechanistic assessment of such a phenomenon in this region. In particular, a thorough investigation on the breaking mechanism and breaking location occurring over the frontal slope of Capo Vaticano is still missing. This information may represent the base for any process-based observational setting, aimed at exploring the link between ISWs breaking and both sedimentary and mixing phenomena occurring over shelf breaks.

In this study, we propose a semi-analytical approach to derive the breaking location of the northward-traveling ISWs, by considering the different breaking mechanisms, as classified through the internal Iribarren number (Aghsaee et al., 2010; Boegman et al., 2005; La Forgia, Adduce, et al., 2018; La Forgia, Tokyay, et al., 2018; Sutherland et al., 2013):

$$Ir = \frac{s}{\sqrt{S_w}}, \quad (1)$$

where $s = \tan(\phi)$ is the topographic slope and $S_w = A/\lambda$ is the wave slope. The Iribarren number is a dimensionless parameter originally applied to define surface gravity wave breaker types on beaches (Dean &

Dalrymple, 1991). Although breaking evolutions of surface and internal waves are rather different, the Irribarren number still allows to define the ISW breaking mechanisms, commonly distinguished in plunging, collapsing, plunging-collapsing, and surging breakers (La Forgia, Adduce, et al., 2018; La Forgia, Tokyay, et al., 2018; Sutherland et al., 2013) (see Section 3). In particular, plunging, collapsing, and plunging-collapsing breaking processes are characterized by the steepening of the trailing wave edge that leads to the verticalization of the wave profile near the breaking point. Our analytical model identifies the ISW breaking location by considering the verticalization of the wave profile, and by adopting two-layer analytical models and the conservation of the wave mass. Laboratory experiments validate our model, and we apply our results to the case of the frontal slope of Capo Vaticano. We then provide a further assessment of our application by performing numerical simulations under real-field conditions.

2. Theoretical Background

The basic model for the description of ISWs in shallow seas is based on the Korteweg-de Vries (KdV) equation:

$$\eta_t + c_0 \eta_x + \alpha \eta \eta_x + \beta \eta_{xxx} = 0, \quad (2)$$

where $\eta(x, t)$ is the pycnocline vertical displacement, c_0 is the phase speed of the associated linear wave, α is the coefficient of the nonlinear term, and β is the coefficient of the dispersive term. The KdV equation for interfacial waves propagating in a two-layer fluid, with a rigid lid and no mean flow, has the following coefficients (Osborne & Burch, 1980):

$$c_0 = \sqrt{\frac{g\sigma h_1 h_2}{h_1 + h_2}}, \quad \sigma = 2 \left(\frac{\rho_2 - \rho_1}{\rho_2 + \rho_1} \right), \quad \alpha = \frac{3}{2} c_0 \frac{h_1 - h_2}{h_1 h_2}, \quad \beta = \frac{c_0}{6} h_1 h_2, \quad (3)$$

where h_1 and h_2 are the lower and the upper layer depths, and ρ_1 , and ρ_2 are the density of the upper and lower layer, respectively, and σ is the layer relative density difference ($\sigma \ll 1$ in Boussinesq approximation). Equation 2 describes a balance between nonlinear effects, which tend to steepen the crest, and linear wave dispersion, which tends to broaden it. Furthermore, Equation 2 is derived under the long wave and small amplitude assumptions, that is, $H/\lambda \ll 1$ and $A/h_1 < 1$.

To describe ISWs of large amplitude, a more suitable model is the extended KdV (eKdV) equation, or Gardner equation, which includes a cubic nonlinearity (Grimshaw et al., 2010; Helfrich & Melville, 2006):

$$\eta_t + \left(c_0 + \alpha \eta + \alpha_1 \eta^2 \right) \eta_x + \beta \eta_{xxx} = 0, \quad (4)$$

where α_1 is

$$\alpha_1 = \frac{3c_0}{(h_1 h_2)^2} \left[\frac{7}{8} (h_1 - h_2)^2 - \left(\frac{h_1^3 + h_2^3}{h_1 + h_2} \right) \right]. \quad (5)$$

A solution of the eKdV equation is

$$\eta(x, t) = \frac{A}{b + (1 - b) \cosh^2 \left[\gamma (x - Ut) \right]}, \quad (6)$$

in which

$$U = c_0 + \frac{A}{3} \left(\alpha + \frac{1}{2} \alpha_1 A \right), \quad \gamma^2 = \frac{A \left(\alpha + \frac{1}{2} \alpha_1 A \right)}{12\beta}, \quad b = \frac{-A\alpha_1}{2\alpha + \alpha_1 A}. \quad (7)$$

The limiting eKdV wave amplitude is given as $\eta_{\max} = -\alpha/\alpha_1$ (Grimshaw et al., 2004; Ostrovsky & Stepanyants, 1989; Small, 2001a; Stanton & Ostrovsky, 1998).

KdV-type models can fail to describe ISW profiles of very large amplitude (e.g., $\eta > \eta_{\max}$). Miyata, Camassa, and Choi derived a strongly nonlinear model able to describe large-amplitude ISWs for a two-layer system under the rigid-lid approximation (Choi & Camassa, 1999; Miyata, 1985), denoted as MCC–RL model. Indeed, for ISWs propagating in stratified ambient fluids with small density differences (as those usually observed in the ocean), the free surface displacements are negligible when compared with the subsurface ones. In particular, to an internal displacement of 50 m, a surface displacement of about 4 cm is predicted by the MCC–FS (Free-Surface) model (Kodaira et al., 2016; La Forgia & Sciortino, 2019). Thus, we can replace the free surface with a rigid boundary. Unlike KdV-type models, in the MCC model, there are no smallness assumptions on wave amplitude.

For a two-layer system, with densities and depths given by ρ_1 and h_1 for the upper fluid layer, ρ_2 and h_2 for the lower layer, and local layer thicknesses,

$$\eta_1 = h_1 - \zeta, \quad \eta_2 = h_2 + \zeta, \quad (8)$$

where ζ is the elevation of the interface, it is possible to derive the following nonlinear ordinary differential equation for ζ (Choi & Camassa, 1999):

$$\zeta_{xx}^2 = \frac{3\zeta^2 [c^2(\rho_1\eta_2 + \rho_2\eta_1) - g(\rho_2 - \rho_1)\eta_1\eta_2]}{c^2(\rho_1h_1^2\eta_2 + \rho_2h_2^2\eta_1)}, \quad (9)$$

where

$$c^2 = \frac{g(h_1 - a)(h_2 + a)(\rho_2 - \rho_1)}{\rho_1h_2 + a(\rho_1 - \rho_2) + \rho_2h_1}. \quad (10)$$

Substituting Equations 8 and 10 into Equation 9, we get the solitary wave profile by numerical integration with the initial condition $\zeta(0) = a$. Integration of Equation 9 through separation of variables is also possible, resulting in a wave profile $\zeta(X)$ expressed by an implicit relation $X = X_s(\zeta)$, where X_s is a combination of elliptic integrals (Choi & Camassa, 1999; Miyata, 1985); wave profiles can be obtained by plotting routines. The depth-averaged velocities in each layer are given as (Choi & Camassa, 1999; Kodaira et al., 2016; La Forgia & Sciortino, 2020):

$$\bar{u}_i = c \left(1 - \frac{h_i}{\eta_i} \right), \quad (11)$$

with $i = 1, 2$ indicating the upper fluid layer and the lower layer, respectively.

An important fully nonlinear and strongly dispersive model we will use in the following is the Dubreil-Jacotin-Long (DJL) model (Dubreil-Jacotin, 1937; Long, 1953). Solitary waves in continuously stratified flows have been explored with numerical solutions (Lamb, 2002; Stasna & Lamb, 2002) of the DJL equation as

$$\nabla^2 \eta + \frac{N^2(z - \eta)}{c^2} \eta = 0, \quad (12a)$$

$$\eta = 0 \text{ at } z = 0, H \quad (12b)$$

$$\eta \rightarrow 0 \text{ as } x \rightarrow \pm\infty, \quad (12c)$$

which is an eigenvalue problem for $\eta(x, z)$, vertical displacement of the streamline passing through (x, z) relative to its far-field height, where $N^2(z) = -gd\bar{\rho}(z) / dz$ is the squared buoyancy frequency, with $\bar{\rho}$ density profile (scaled by the reference density ρ_0), and H is the total depth. The equation is solved through a generalization of the variational technique and a numerical algorithm based on the works of Turkington et al. (1991) and Dunphy et al. (2011). In the algorithm neither the wave amplitude, nor the wave propagation speed is specified. Instead, the kinetic energy of the disturbance is minimized under the constraint that the available potential energy (scaled by ρ_0gH)

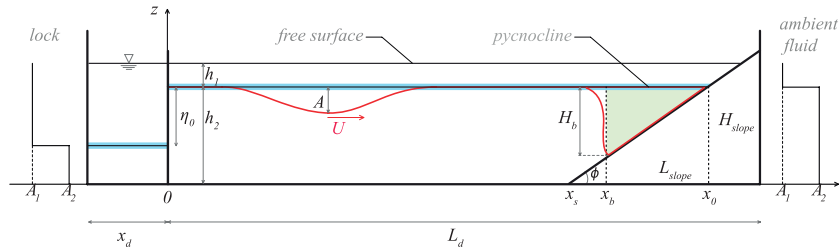


Figure 2. Experimental setting: h_1 and h_2 , top layer and bottom layer thicknesses, respectively; η_0 , pycnocline displacement between lock region and ambient region; ϕ , slope angle; H_{slope} and L_{slope} , height and length of the slope, respectively; x_s , abscissa of the toe of slope; x_0 , abscissa of the point of intersection between the pycnocline and the slope; x_d , length of the lock region; L_d , length of the ambient fluid region.

$$\text{APE}(\eta) = \frac{1}{H} \int_0^H \int_{-\infty}^{+\infty} \int_0^\eta [\bar{\rho}(z - \eta) - \bar{\rho}(z - s)] ds dx dz, \quad (13)$$

is held fixed (Dunphy et al., 2011; Xu & Stastna, 2019). In contrast with weakly nonlinear theories, which are approximate, solutions found by using the variational technique are exact solutions of Euler's equations. However, these solutions cannot be used for direct analytic manipulation, since they are not explicit.

3. Modeling ISWs Breaking Location

3.1. Experimental Setting for ISWs Breaking

To investigate the interaction between a single ISW and a sloping boundary, we generate different types of ISWs by the lock-release method (Kao et al., 1985) in a 3.0 m long, 0.2 m wide, and 0.3 m deep Perspex tank (Figure 2). The entire domain is initially filled with a solution of sodium chloride (NaCl), generating the lower layer of uniform density ρ_2 . Over the free surface, we add fresh water of uniform density $\rho_1 < \rho_2$ (La Forgia, Adduce, et al., 2018; La Forgia, Tokyay, et al., 2018). We then insert a vertical gate at a distance x_d from the left wall of the tank (Figure 2), making sure that its bottom is a few millimeters above the channel bottom. Thus, adding further fresh water on the free surface of the lock, a known volume of brine water flows below the gate, reestablishing the hydrostatic equilibrium. During this phase, the pycnoclines of the two regions form the displacement η_0 , which represents the initial setting of the runs. It therefore results in a two-layer stratification, composed of a thin, upper layer of fresh water of thickness h_1 and a lower, denser layer of thickness $h_2 > h_1$; the pycnocline is deeper within the lock region, where the thickness of the lighter fluid is $h_1 + \eta_0$ (Figure 2). The gravity collapse induced by the gate removal leads to the generation of a single ISW of depression propagating downstream, toward an inclined surface with a slope angle ϕ . We use a digital camera to record the flow evolution from the lateral wall of the tank. By the instantaneous pycnocline position inferred by image analysis, we estimate the wave amplitude A , the characteristic wavelength λ , the wave surface S , and the wave celerity c .

Depending on the ISW geometric features and slope inclination (i.e., the Iribarren number), the wave shoaling over the sloping boundary develops differently. Each breaking mechanism is consequently characterized by different effects in terms of mixing, entrainment, and shear stress over the bottom (La Forgia, Tokyay, et al., 2020). During the wave shoaling, two main processes occur: the steepening of the rear edge of the wave and the downward motion of the volume confined between the leading edge of the wave and the sloping boundary.

For plunging breakers, a dominant steepening of the trailing edge of the wave takes place, followed by a quick clockwise overturning in the onshore direction, inducing strong local mixing. For collapsing breakers, the downward motion of the confined fluid results to be dominant, compared with the trailing edge steepening: the trapped dense fluid leaves its original position with a fast downward motion in the adverse pressure gradient region. As a result, a turbulent separated bolus forms and quickly dissipates. Then, a part of the incident wave is reflected and a gravity current composed of the denser fluid flows up the slope, until hydrostatic conditions are reestablished. An intermediate breaking mechanism, that is, the plunging-collapsing

breaker, is observed when the two main shoaling processes occur in the breaking location. Finally, in the case of surging breakers, ISWs are not subject to any observable large-scale instability during the shoaling until the wave trough reaches the sloping bottom. The wave is almost reflected by the right wall of the tank (La Forgia, Adduce, et al., 2018; La Forgia, Tokyay, et al., 2018).

The occurrence of a particular kind of breaking mechanism depends on the geometry of the incident waves and slope angle. Different types of breaking are commonly distinguished introducing the internal Iribarren number (Ir) (Aghsaee et al., 2010; Boegman et al., 2005; Sutherland et al., 2013). For $Ir < 1$ plunging breakers and for $Ir = 1 \div 1.5$ collapsing breakers are observed, while plunging-collapsing breakers occur for $Ir \simeq 1$. Surging breakers occur for $Ir > 1.5$ (La Forgia, Adduce, et al., 2018; La Forgia, Tokyay, et al., 2018). Our experiments well reproduce plunging, collapsing, and plunging-collapsing breakers, which are the most relevant breaking mechanisms expected in the continental shelf region.

3.2. Wave-Breaking Conceptual Model

In experiments with plunging, collapsing, and, in particular, plunging-collapsing breakers, the solitary wave evolves so that, near the breaking point, the interface between the two fluids is nearly vertical, where it intersects the slope at its point of maximum descent (see Figure 2). Since the wave assumes a right-angled triangular shape in the rightmost corner of the tank, we estimate the area (volume per width) of the fluid below the initial depth of the interface as (Sutherland et al., 2013)

$$S_{tr} \simeq \frac{H_b L_b}{2} = \frac{H_b^2}{2s}, \quad (14)$$

where $L_b = x_0 - x_b$ is the distance between x_b , x_0 is the point where the slope intersects the unperturbed interface, and H_b is the maximum displacement of the interface (Figure 2).

By imposing that the fluid mass, transported by the initial soliton, is approximately the mass contained in the pre-breaking “trianglized” soliton (Figure 2), we equate Equation 14 to the area of the soliton at $t = 0$. An analytical estimation of the area enclosed by the soliton can be derived through eKdV theory:

$$S_{eKdV} = \int_{-\infty}^{+\infty} \frac{A}{b + (1-b)\cosh^2(\gamma x)} dx. \quad (15)$$

By multiplying and dividing the integrand by $\text{sech}^2(\gamma x)$, and considering that $\text{sech}^2(\gamma x) = 1 - \tanh^2(\gamma x)$, we get

$$S_{eKdV} = 2A \int_0^{+\infty} \frac{\text{sech}^2(\gamma x)}{1 - b \tanh^2(\gamma x)} dx,$$

which can be integrated via the substitution $t = \tanh(\gamma x)$:

$$S_{eKdV} = \frac{2A}{\gamma} \int_0^1 \frac{dt}{1 - bt^2} = \frac{A}{\sqrt{b}\gamma} \log \left(\frac{1 + \sqrt{bt}}{1 - \sqrt{bt}} \right) \Big|_0^1 = \frac{2A \tanh^{-1}(\sqrt{b})}{\sqrt{b}\gamma}, \quad (16)$$

where we used the identity

$$\tanh^{-1}(\sqrt{b}) = \frac{1}{2} \log \left(\frac{1 + \sqrt{b}}{1 - \sqrt{b}} \right),$$

valid for $|\sqrt{b}| < 1$. By equating Equation 14 to Equation 16, that is, $S_{tr} = S_{eKdV}$, we obtain

$$\frac{H_b^2}{2s} = \frac{2A \tanh^{-1}(\sqrt{b})}{\sqrt{b}\gamma} \Rightarrow H_{bcKdV} = \sqrt{\frac{4As \tanh^{-1}(\sqrt{b})}{\sqrt{b}\gamma}}. \quad (17)$$

Using Equation 17, we derive an expression for the breaking point x_b , evaluated with respect to the toe of slope x_s (i.e., the intersection point between the slope and the horizontal bottom):

$$x_0 - x_b = \frac{H_b}{s} \Rightarrow x_{beKdV} = x_0 - \frac{H_b}{s} = \frac{h_2}{s} - \sqrt{\frac{4A \tanh^{-1}(\sqrt{b})}{s\sqrt{b}\gamma}},$$

where h_2 is the height of the intersection between the slope and the unperturbed interface. If we set the origin of the system in O as in Figure 2, we have

$$L_{\text{slope}} = \frac{H_{\text{slope}}}{s},$$

and it is possible to derive x_s as

$$x_s = L_d - L_{\text{slope}} = L_d - \frac{H_{\text{slope}}}{s},$$

where L_d is the extent of ambient fluid region, and L_{slope} and H_{slope} are the length of the projection of the slope on the x and the z axes, respectively (Figure 2). Thus, to evaluate x_b with respect to O , we rewrite the breaking point as:

$$\tilde{x}_{beKdV} = x_s + x_{beKdV} = x_s + \frac{h_2}{s} - \sqrt{\frac{4A \tanh^{-1}(\sqrt{b})}{s\sqrt{b}\gamma}}. \quad (18)$$

An equivalent estimation can be performed through the MCC theory. In fact, once obtained the wave profile $\zeta = \zeta(X)$, we can integrate numerically ζ over a large interval ($\zeta \rightarrow 0$ for $X \rightarrow \pm\infty$) to get the area enclosed by the soliton, and we can set

$$S_{\text{MCC}} \approx \frac{H_b^2}{2s},$$

and we obtain

$$H_{b\text{MCC}} = \sqrt{2S_{\text{MCC}}s}, \quad x_{b\text{MCC}} = \frac{h_2}{s} - \sqrt{\frac{2S_{\text{MCC}}}{s}}. \quad (19)$$

The theoretical internal Iribarren number is then obtained by writing the wavelength λ as

$$\lambda = \frac{S}{A} \Rightarrow \text{Ir} = \frac{s}{\sqrt{A/\lambda}}, \quad (20)$$

where the wave surface S can be set equal to S_{eKdV} or S_{MCC} , that is, Equation 16 and the numerical result from the MCC profile integration, respectively.

3.3. Experimental Results and Model Validation

We here compare the experimental and theoretical wave profiles during the propagation phase of (a) plunging, (b) collapsing, and (c) plunging-collapsing breakers (Figure 3). We analyzed six different cases, whose experimental parameters are reported in Table 1.

The KdV model does not fit well the experimental data, since the ISWs generated in the tank are strongly nonlinear (dashed blue line in Figures 3a–3c). In the case of plunging breakers, in particular, the amplitude of the experimental wave profile exceeds the maximum amplitude admitted for eKdV waves. For cases (2) and (3), the eKdV profile fits well the experimental ones, although the latter profile appears slightly broader (yellow dot-dashed lines in Figures 3b and 3c). The MCC strongly nonlinear model provides the best agreement with the experimental waves for all cases (red lines in Figures 3a–3c).

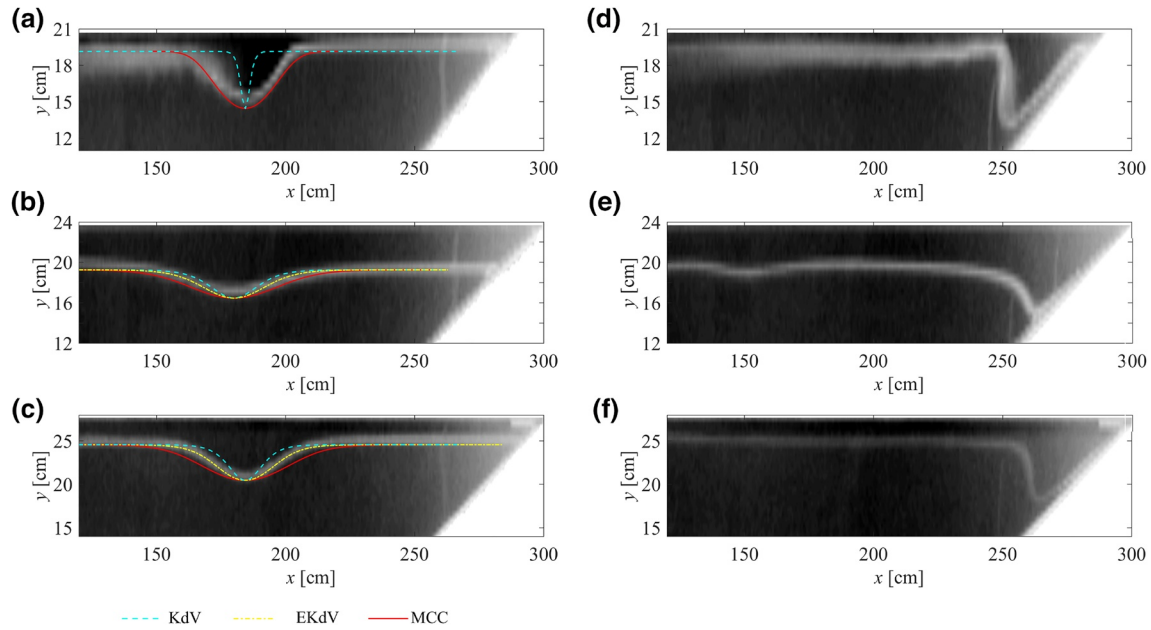


Figure 3. Comparison between experimental and theoretical wave profiles for (a) plunging breaker, (b) collapsing breaker, and (c) plunging-collapsing breaker during free propagation phase. In (d–f), experimental profiles corresponding, respectively, to cases (a), (b), and (c) at verticalization instant.

Experimental waves are observed to shoal over sloping boundary, leading to the trailing edge steepening. By image analysis, we obtain the maximum breaking depth H_b and location x_b , associated to the trailing edge verticalization (see Figures 3d–3f). We then apply the model described in Section 3.2 to derive the theoretical breaking locations. We report the comparison between the experimental and theoretically predicted values for \tilde{x}_b in Table 1. The good agreement between the experiments and our theoretical model (Figure 3 and Table 1) suggests that the adopted geometrical approximations, based on the mass conservation and the observed shoaling evolution, is suitable for predicting breaking location for a given ISW, once the topographic features are known. Moreover, the comforting agreement between both eKdV and MCC models and the laboratory simulations suggests that friction effects should not play a significant role in the prediction of ISW breaking location.

Our results are consistent with those obtained by empirical criteria proposed in previous studies (Helfrich, 1992; Massel, 2015; Vlasenko & Hutter, 2002). Laboratory experiments by Helfrich (1992) showed that wave breaking occurs when normalized maximal wave height $a_m/(H_b - H_m)$ exceeds 0.4 and does not depend on the bottom slope, that is,

$$\frac{a_m}{H_b - H_m} \geq 0.4. \quad (21)$$

where a_m is the maximum displacement at the center of wave, H_b is the water depth at point of wave breaking, and H_m is the depth of an undisturbed position of the interface line (Massel, 2016). Numerical calculations by Vlasenko and Hutter (2002) showed that the kinematic instability is responsible for mechanisms of strong wave breaking rather than a shearing instability. They considered a two-layer system with a vertical fluid stratification. Amplitudes of waves and the bottom parameters were chosen to be close to those observed in the Andaman and Sulu Seas. A proposed breaking criterion for ISWs for sea bottom slope in the range of $0.52^\circ < \gamma < 21.88^\circ$ is

$$\frac{a_m}{H_b - H_m} \geq \frac{0.8^\circ}{\gamma} + 0.4. \quad (22)$$

If the water depth on the shelf is less than H_b , a solitary wave breaks before it and penetrates into the shallow water zone; otherwise, it passes into the shelf without breaking.

Table 1

Experimental Parameters and Comparison Between Experimental and Theoretical Values for \tilde{x}_b , in the Case of (a) Plunging, (b) Collapsing, (c) Plunging-Collapsing

Case	h_1 (cm)	h_2 (cm)	$\Delta\rho$ (g/cm ³)	A (cm)	S	Ir	x_s (cm)	$\tilde{x}_{b\text{exp}}$ (cm)	$\tilde{x}_{b\text{eKdV}}$ (cm)	$\tilde{x}_{b\text{MCC}}$ (cm)	$\tilde{H}_{b\text{exp}}$ (cm)	$\tilde{H}_{b\text{eKdV}}$ (cm)	$\tilde{H}_{b\text{MCC}}$ (cm)	$H_{b\text{Helfrich}}$ (cm)	$H_{b\text{VH}}$ (cm)
(a)	0.96	20.40	0.028	4.7	0.296	0.61	216.8	249.7	–	256.5	8.56	–	9.60	12.71	11.44
(b)	3.50	20.50	0.032	2.13	0.296	1.16	216.2	258.6	263.5	260.4	9.40	9.06	10.92	8.82	8.25
(c)	2.83	25.17	0.033	4.1	0.341	1.00	217.1	260.4	265.5	259.5	10.29	11.64	13.53	13.08	12.09
(a)	3.23	16.61	0.030	5.23	0.203	0.53	201.0	223.0	–	233.1	9.92	–	13.41	16.30	14.34
(a)	3.44	16.56	0.030	4.45	0.360	0.84	204.0	219.2	217.3	216.2	10.39	14.49	15.57	14.56	13.54
(a)	2.30	18.00	0.030	4.1	0.203	0.52	207.4	248.4	262.6	258.8	7.70	8.93	9.83	12.55	11.03

Notes. h_1, h_2 , layer thicknesses; $\Delta\rho = \rho_2 - \rho_1$, density difference; A , wave amplitude; s , topographic slope; Ir , Iribarren number; x_s , toe of slope abscissa; $\tilde{x}_{b\text{exp}}$ and $\tilde{H}_{b\text{exp}}$, experimental breaking location and depth; $\tilde{x}_{b\text{eKdV}}, \tilde{H}_{b\text{eKdV}}$ and $\tilde{x}_{b\text{MCC}}, \tilde{H}_{b\text{MCC}}$, theoretical breaking locations and depths from eKdV and MCC theory, respectively. $\tilde{H}_b = h_1 + H_b$ for the eKdV and MCC cases.

In Figure 4, we propose a comparison between our analytical breaking model and the breaking criteria of Helfrich and Vlasenko-Hutter using our experimental data. We observe that our analytical model better agrees with the experimental breaking depths if we consider eKdV solutions for collapsing and plunging-collapsing breakers, and the MCC model for plunging breakers.

4. Assessment for Real-Field Conditions

4.1. ISWs Refraction Off Capo Vaticano Frontal Slope

Refraction causes waves to bend differently depending on slopes and irregularities characterizing the bottom topography. This happens because the wave velocity decreases with depth, so that the portion of the crest nearer the shore moves slowly, while the portion of the crest in deeper water races ahead (Dean & Dalrymple, 1991; Munk & Traylor, 1947).

Furthermore, wave refraction can modify the shoaling process, leading to faster wave-breaking and enhancing water mixing and turbulent processes near shallow areas (Alpers & Vlasenko, 2019; Vlasenko & Stashchuk, 2007). Usually, wave refraction processes are studied numerically through two-dimensional simulations (Cai & Xie, 2010) or ray tracing techniques (T. Jia et al., 2017; Small, 2001b; Xie et al., 2015). However, to study ISW refraction near the Capo Vaticano frontal slope, here we adopt an extension of the procedure provided by Droghei et al. (2016), which reduces the need for numerical simulations. The procedure involves using Snell's law (Pelinovsky et al., 1994):

$$\frac{\sin \theta}{C} = \frac{\sin \theta_0}{C_0} = K_s, \quad (23)$$

where θ is the angle between wave crest and depth contour at an arbitrary depth, θ_0 is the angle between wave crest and depth contour in deep water, C is the wave celerity at an arbitrary depth, and C_0 is the wave celerity in deep water. Snell's law indicates that for coastlines with straight and parallel contours, shoaling waves tend to approach the shoreline normally (Dean & Dalrymple, 1991; Munk & Traylor, 1947; Sutherland, 2010).

For our application, by choosing a set of points on the initial wave front, we identify the different wave rays (T. Jia et al., 2017; Small, 2001b) and

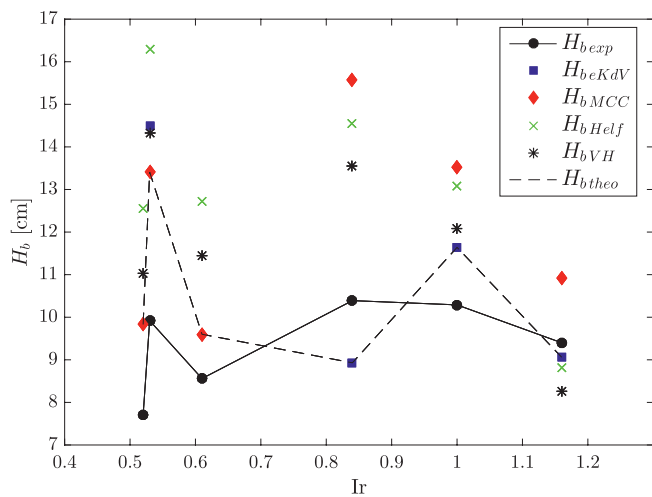


Figure 4. Comparison between our analytical prediction ($\tilde{H}_{b\text{theo}}$) of the breaking depths and the criteria of Helfrich (21) and Vlasenko-Hutter (22) with respect to experimental data ($\tilde{H}_{b\text{exp}}$). The analytical model seems to reproduce quite well the experimental values using eKdV predictions (blues squares) for collapsing and plunging-collapsing breakers, and MCC model (red diamonds) for plunging breakers.

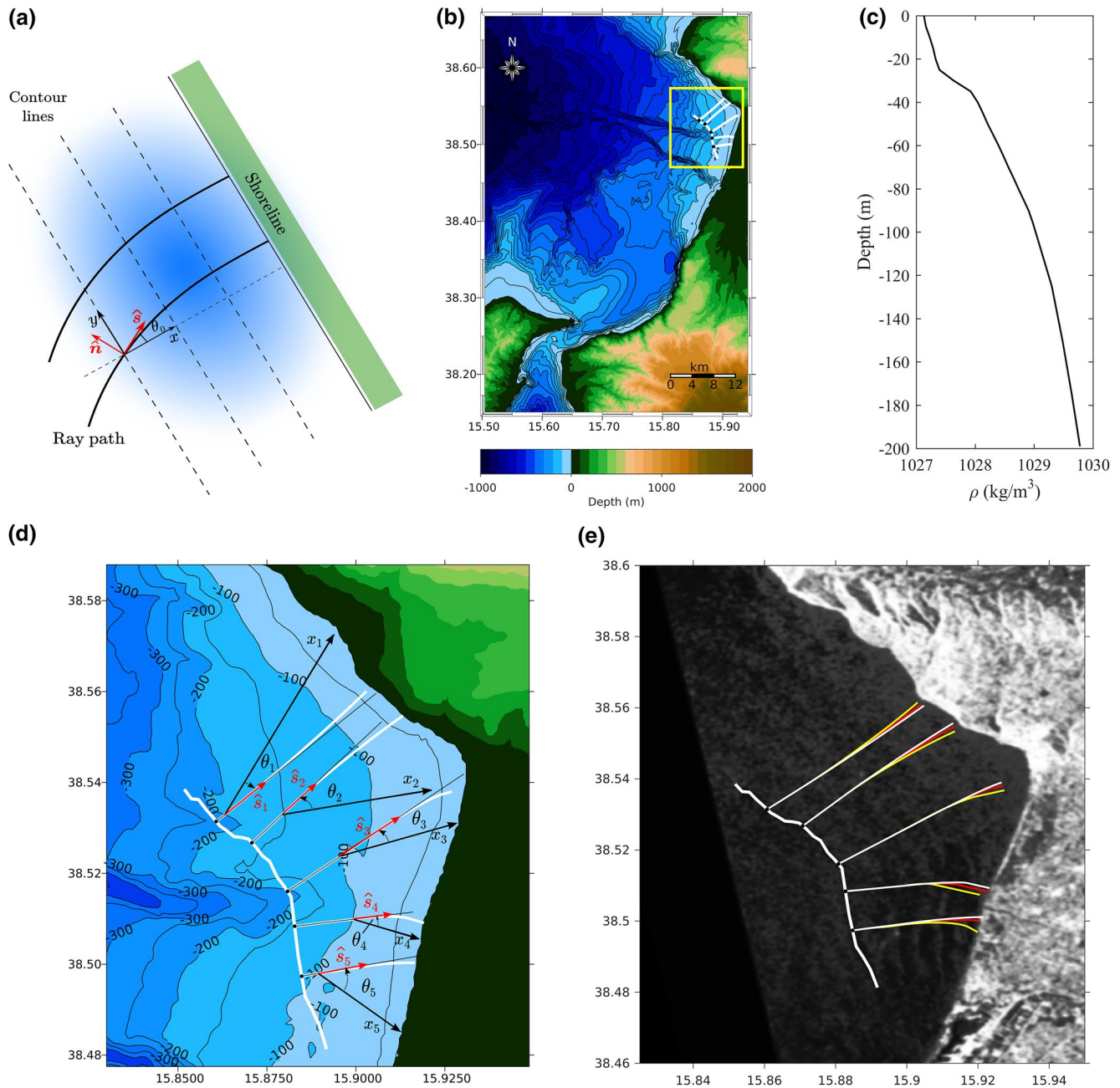


Figure 5. (a) Schematic representation of the interaction between a wave ray and the bathymetry. A ray is drawn from deep water location to the first intersection of a contour. The normal to the contour line, with direction x , allows to calculate the angle of incidence θ_0 . \hat{s} and \hat{n} are tangent and the normal to the wave ray, respectively. (b) The yellow box indicates the area of interest for our wave-refraction calculations. A wave front from Sentinel 1A on May 10, 2019 (see also (e)) is reported. (c) Mean stratification of May at 38.5°N 15.75°E from World Ocean Atlas 2018; we consider the pycnocline as positioned at 35 m. (d) Magnification of the highlighted area in (b). White lines: wave front and refracted wave trajectories $y_i(x)$, $i = 1, \dots, 5$, calculated through (26). (e) Superimposition of the refracted wave trajectories on the observed front for $h_1 = 35$ m (white line), $h_1 = 60$ m (red line), $h_1 = 75$ m (yellow line).

we decompose the wave vector with direction \hat{s} (tangent to the wave ray) in two orthogonal components along x and y (Dean & Dalrymple, 1991; see Figure 5); it results that

$$\frac{ds}{dt} = C, \quad \frac{dx}{dt} = C \cos(\theta), \quad \frac{dy}{dt} = C \sin(\theta). \quad (24)$$

By assuming an initial angle of incidence θ_0 , and thus K_s , from Equation 23, we have $\sin(\theta) = CK_s$, $\cos(\theta) = \sqrt{1 - C^2 K_s^2}$, and from Equation 24, we can derive the following first-order differential equation:

$$\frac{dy}{dx} = \tan(\theta) = \frac{K_s}{\sqrt{\frac{1}{C^2(x)} - K_s^2}}, \quad C(x) = \sqrt{\frac{g\sigma h_1 h_2(x)}{h_1 + h_2(x)}}, \quad (25)$$

where we assume that the linear long wave celerity C depends on a slowly varying bottom layer $h_2(x)$ (the upper layer h_1 is kept constant). Equation 25 gives the refracted wave trajectory:

$$y(x) = \int_{x_0}^x \frac{K_s}{\sqrt{\frac{1}{C^2(x)} - K_s^2}} dx. \quad (26)$$

We then apply Equation 26 to the wave front observed by Sentinel 1A on May 10, 2019 (Figure 5b), considering the climatological monthly mean stratification of May, from World Ocean Atlas 2018 (Figure 5c), which indicates a pycnocline at about $h_1 = 35$ m. This allows us to calculate the refracted trajectories $y_i(x)$ through Equation (26), making use of the real bathymetric profiles along x_i (Figures 5d and 5e). The resulting trajectories tend to bend slightly becoming gradually orthogonal to the shallowest contour lines (Figures 5d and 5e); this remains valid also considering different h_1 values. From Figure 5e, we notice that the position of the pycnocline seems to have a small influence on the overall process. Our analysis motivates the ansatz of considering ISWs arriving almost orthogonal to isobaths south of Capo Vaticano (see Section 5).

4.2. Effects of Real-Field Stratification and Geometry on ISWs

Density distribution along the water column characterizes ISW features not only during their interaction with the bottom, but also during their free propagation (Ottolenghi et al., 2020). To take into account real-field stratification effects for ISWs propagating in a steady state, we make use of the DJL equation (Figure 6). Numerical simulations will then be compared with the MCC semi-analytic results in order to assess the reliability of our theoretical prediction under realistic settings. In particular, we investigate those ISWs that are able to induce surface manifestations in the Gioia Basin, that is, those occurring during late spring and summer (Brandt et al., 1999), and that are expected to be the most energetic in terms of bed shear stress.

To run DJL simulations, we schematize two different water stratifications, characterized by half-pycnocline thicknesses h_p of 10 and 20 m, respectively (see solid and dashed lines in Figure 6e), from the unperturbed density profile in Figure 5c. We appropriately set the APE values as $APE_1 = 5.0 \times 10^3 \text{ m}^4/\text{s}^2$ for $h_p = 10$ m and $APE_2 = 4.3 \times 10^3 \text{ m}^4/\text{s}^2$ for $h_p = 20$ m, in order to compare the density and velocity fields for ISWs with the same realistic amplitude, that is, $A = 47.1$ m (Brandt et al., 1999). From the two resulting density fields (Figures 6a and 6c), we obtain the DJL ISW profiles, defined by the mean iso-density line $\rho_m = (\rho_1 + \rho_2)/2$ (see solid lines in Figures 6a and 6c). Wave profiles predicted by the DJL simulations under two different pycnocline thicknesses appear in good agreement with those obtained from the MCC semi-analytic model (see dashed lines in Figures 6a and 6c). This confirms that the pycnocline thickness does not significantly affect the ISWs geometrical features, which can be therefore predicted by the simpler two-layer interfacial models, as the MCC (La Forgia, Ottolenghi, et al., 2020). In this context, since the Iribarren number directly depends on the ISW amplitude and wavelength, the related breaking criteria are expected to be weakly affected by the intermediate layer thickness (Aghsaei et al., 2010), as assessed by our DJL simulations (Figures 6a and 6c). Thus, the ISW breaking mechanism can be easily obtained by considering the simplified and associated density structure (i.e., h_1 , h_2 , ρ_1 , and ρ_2).

The intermediate layer thickness mostly affects the ISW kinematics. For a thinner pycnocline, indeed, an ISW propagates slightly faster, being $c_{\text{DJL}} = 0.871$ m/s for $h_p = 10$ m, and $c_{\text{DJL}} = 0.809$ m/s for $h_p = 20$ m (Figures 6a–6d, respectively). For both cases the MCC model predicts a celerity of $c_{\text{MCC}} = 0.95$ m/s, significantly larger than those resulting from the DJL equation. Two-layer interfacial models overestimate the wave celerity, which is strongly affected by the actual intermediate layer thickness. Moreover, larger horizontal velocities can be observed nearby the maximum pycnocline displacement, where the velocity magnitudes

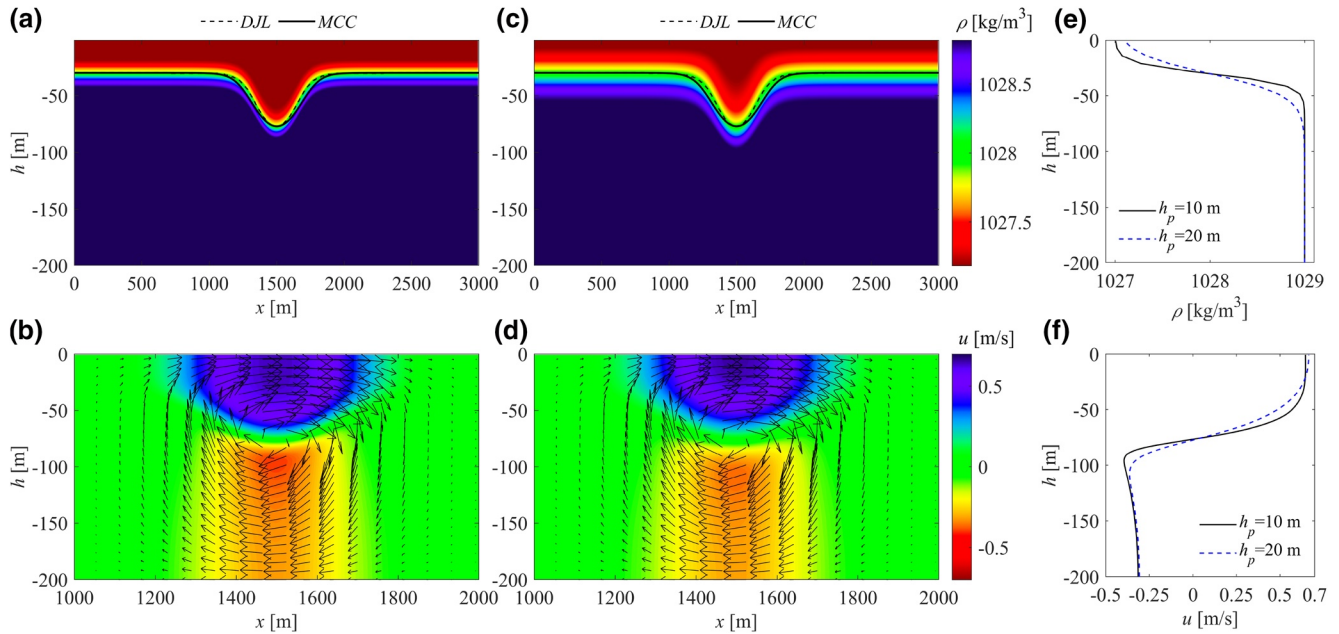


Figure 6. Numerical solution of the DJL equation for a 3-km long and 0.2-km high domain with a 30-m depth pycnocline. Predicted (a, c) density and (b, d) horizontal velocity fields for ISWs with the same amplitude ($A = 47.1$ m), propagating through (e) two undisturbed density profiles having different half-pycnocline thicknesses ($h_p = 10$ m and $h_p = 20$ m, respectively). Vectors show the associated velocity fields. Dashed and solid lines in (a and c) refer to the ISW profiles predicted by the MCC and DJL models, respectively. (f) Horizontal velocity profiles predicted at the maximum pycnocline displacements.

are larger (compare the regions at $x = 1,500$ m and $h \simeq -100$ m in Figures 6b and 6d). However, far from the interface, the predicted horizontal velocities assume approximately the same value ($u \simeq 0.31$ m/s in Figure 6f).

5. ISWs Breaking Location Over the Frontal Slope of Capo Vaticano

ISWs generated at the sill of the Messina Strait modify their features when they interact with bathymetric constraints. SAR images allow us to visualize the path of the surface manifestations of ISW packets propagating northward from the Messina Strait (Figure 1b). We observe, in particular, three different ISW packets, produced at the sill at approximately every 12 h (F1–F3 in Figure 1b), and wave refraction phenomena close to topographic mounds and coastlines (see F1–F2 in Figure 1b), which tend to deflect wave trajectories toward shallow areas (Droghei et al., 2016).

Interestingly, south of the Capo Vaticano coastline, no relevant surface manifestation of ISWs is visible, while the ISWs packet F3 keeps propagating westward (Figure 1b). This suggests an interaction between the northward-propagating ISWs and the Capo Vaticano frontal slope, which induces wave breaking, as marked by observation of the thermal front and the dark gray area southward of Capo Vaticano (Marullo & Santoleri, 1986).

To apply our theoretical approach for predicting breaking location on real field, we consider ISWs arriving orthogonal to isobaths over the steeper slope south of Capo Vaticano (Figure 7), in accordance with the refracting properties of ISWs (see Section 4.1). We then set in Equations 4 and 9, the following water column stratification conditions: $H = h_1 + h_2 = 400$ m, with $\rho_1 = 1026$ kg/m³, $\rho_2 = 1029$ kg/m³. To take into account the seasonal effects, we consider two pycnocline locations: $h_1 = 30$ m (Alpers & Salusti, 1983; Sapia & Salusti, 1987) and $h_1 = 70$ m (Brandt et al., 1999). Slopes have been linearized in $0 \div 300$ m depth. By considering ISW amplitudes that range from $A = 40$ m to $A = 70$ m (Brandt et al., 1999), we estimate the breaking depths H_b and the theoretical values for the Iribarren number for each case (Figure 7). The Iribarren numbers are in the range $Ir \simeq 0.15 \div 0.80$, consistent with a plunging breaking mechanism. For each incoming wave and slope direction, we define the breaking position as the location where ISWs are expected to verticalize. The resulting breaking depths are in the range of $H_b \simeq 50 \div 200$ m and the distance from the coastline varies

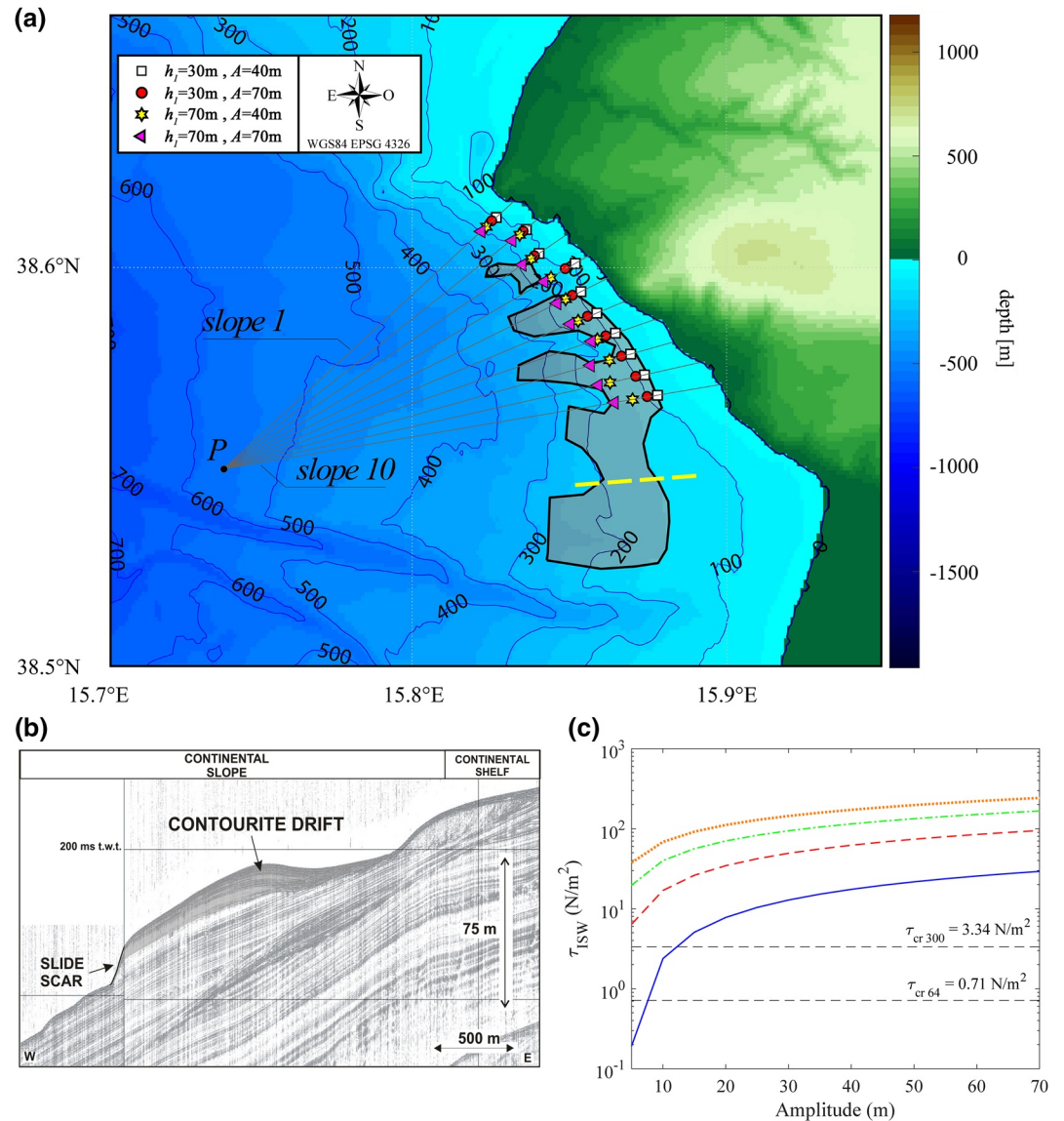


Figure 7. (a) Breaking positions (symbols) and related depths along each slope from the MCC theory. Breaking points from eKdV (not shown) are located really close to the respective MCC points. The identified breaking depth results to be in the range of $H_b \approx 50 \div 200$ m and the distance from the coastline varies approximately from 2 to 4 km. Lines represent ISW pathways over the steeper slopes south of Capo Vaticano. The shaded area indicates the contourite zone reported in Figure 1d, in order to highlight the agreement between breaking point locations and morpho-bathymetric features. (b) Representative seismic profile across the continental slope off Capo Vaticano (see dashed yellow line in Panel a) showing contourite drift deposits truncated by a slide scar on the seaward flank (modified from Martorelli et al., 2016). (c) Values of the bed shear stress τ_{ISW} induced by ISWs, calculated through relation (28) for different values of A and h_1 . Blue solid line, $h_1 = 10$ m; red dashed line, $h_1 = 30$ m; green dot-dashed line, $h_1 = 50$ m; orange dotted line, $h_1 = 70$ m. The critical bed shear stresses $\tau_{cr,64}$ and $\tau_{cr,300}$ are evaluated inverting (30) for $\Theta_{ISW} = 0.7$, and for $d_{50} = 64 \mu\text{m}$ and $d_{50} = 300 \mu\text{m}$, respectively.

approximately from 2 to 4 km (Figure 7). The trailing edge verticalization is associated to the larger offshore bottom velocities, induced by the downslope flow of the denser water beneath the leading edge (Aghsaee et al., 2010). In this bathymetric strip, we then expect to observe phenomena that are associated with the shoaling and breaking of ISWs, such as turbulent mixing and sediment resuspension, that likely modify the seafloor morphology (Cacchione et al., 2002; Ma et al., 2016).

Numerical (Aghsaee et al., 2012; Bourgault et al., 2014), laboratory (Aghsaee & Boegman, 2014; Boegman & Ivey, 2009), and field (Bluteau et al., 2016; Quaresma et al., 2007) studies indicate that ISWs can force enough bottom shear stress to suspend sediments. For this, two main conditions need to be satisfied: (1) the flow must generate a sufficient bottom shear stress to create incipient sediment motion at the bed (van Rijn, 1993) and (2) the flow must induce near-bed vertical velocities large enough to detach sediments and eject them into the water column (Boegman & Ivey, 2009; van Rijn, 1993). The contribution of bed shear stress to sediment resuspension is typically assessed by using the Shields parameter, that is, the ratio between the force acting to move a grain on the bed to the submerged weight of the grain that counteracts this force (Quaresma et al., 2007; Soulsby, 1997):

$$\Theta = \frac{\tau_b}{(\rho_s - \rho_f)gd_{50}}, \quad (27)$$

where τ_b is the bed shear stress, ρ_s is the sediment density, ρ_f is the fluid density at the bed, and d_{50} is the median grain size. To develop an ejection-based resuspension parameterization for ISWs on a flat bottom, Aghsaee et al. (2012) defined a sediment lifting bed stress

$$\tau_{\text{ISW}} = \rho_2 w_{\text{max}}^2 = \rho_2 c_0^2 [0.09 \ln(Re_{\text{ISW}}) - 0.44]^2, \quad (28)$$

where w_{max} is the maximum instability-driven vertical velocity within the jet, ρ_2 is the lower layer density, and Re_{ISW} is the momentum thickness Reynolds number defined as

$$Re_{\text{ISW}} = |U_2| \sqrt{L_w / [\nu(|U_2| + c)]}, \quad (29)$$

where U_2 is the velocity of the fluid in the bottom layer, c is the phase velocity, ν is the kinematic viscosity, and L_w is the characteristic wavelength defined as in Equation 20.

Using τ_{ISW} in Equation 27, we obtain a Shields-type criterion for resuspension beneath ISWs (Aghsaee & Boegman, 2014; Aghsaee et al., 2012):

$$\Theta_{\text{ISW}} = \frac{\rho_2 w_{\text{max}}^2}{(\rho_s - \rho_2)gd_{50}} = \frac{\rho_2 c_0^2 [0.09 \ln(Re_{\text{ISW}}) - 0.44]^2}{(\rho_s - \rho_2)gd_{50}} \gtrsim 0.7. \quad (30)$$

Resuspension takes place when Θ_{ISW} is higher than the critical value $\Theta_{cr} = 0.7$. To give an estimation of τ_{ISW} in our case, we set in Equation 29 $\nu = 10^{-6} \text{ m}^2/\text{s}$, $\rho_s = 2650 \text{ kg/m}^3$ (quartz particles), and we evaluate $|U_2|$ and c through the MCC model, that is, through Equations 10 and 11, respectively (Figure 7c). We consider the values for d_{50} near the Capo Vaticano frontal slope (highlighted area in Figure 1d) in the range $64 \div 300 \mu\text{m}$ (Martorelli et al., 2021). The criterion (Equation 30) is valid only over a flat bottom, but as observed in numerical (Aghsaee et al., 2010; La Forgia, Tokyay, et al., 2020) and experimental studies (Michallet & Ivey, 1999), when the wave interacts with the slope, the bottom-induced current increases rapidly, increasing both the bottom shear stress and the sediment resuspension. Then the wave becomes distorted and breaks, and the near-bottom vertical velocity assumes relatively large values. Thus, imposing $\Theta_{\text{ISW}} = 0.7$ in Equation 30, we can derive a critical value τ_{cr} , which represents a lower bound for the bottom shear stress that is needed to induce sediment resuspension for a wave shoaling and breaking over a slope. From our analysis, since the ISW-induced bed shear stress results to be considerably larger than the associated critical values (Figure 7c), we argue that waves breaking may contribute to sediment resuspension in the strip area near Capo Vaticano.

Although we have no clear evidence of a mechanistic link between ISWs and the large-scale morpho-sedimentary features south of Capo Vaticano, the occurrence and the specific location of breaking processes we infer from our predicting analytical tool suggests an active role of ISW breaking in resuspending sediment and thus contributing in reshaping, here, the seafloor. Therefore, ISW-induced effects might be superimposed in both alongslope and downslope sedimentary processes (described by Martorelli et al., 2016, 2021) that affect the seabed. In this regard, the most likely interactions between ISWs and the seabed would be related

to the additional bed shear stress, produced by ISW breaking, which leads to an enhancement of sediment resuspension, as well as seabed erosion and instability (see Y. Jia et al. (2019), and references therein). In particular, during the shoaling process, intense near-bottom velocities can erode seafloor sediments and generate nepheloid layers, intruding offshore (Bourgault et al., 2014; Dickson & McCave, 1986). In our case, resuspension may represent a favorable factor for formation of contourite deposits, by providing available resuspended sediment that can be shaped by the alongshore current, and may contribute to net downslope sediment flux. Moreover, ISWs breaking might be also considered as an additional triggering mechanism for slope failures of recent deposits, as observed in the Luzon Strait, between Taiwan and the Philippines (Gavey et al., 2017; Shanmugam & Wang, 2015).

6. Conclusion

In this study, we proposed a semi-analytical method to derive the breaking location of ISWs interacting with a sloping bathymetry. Our theoretical model, based on KdV-type models, MCC theory, mass conservation, and shoaling evolution observations, agrees very well with the laboratory experimental data for the breaking location. By applying this theoretical model to the real-field case of the frontal slope south of Capo Vaticano, we identified an area where ISWs are expected to break. This result is indirectly confirmed by SAR imagery and by past field observations performed in the area. Our analysis on refractive effects shows that the wave fronts revealed by SAR images tend to interact orthogonally with the frontal slope of Capo Vaticano. We also assess the reliability of the MCC two-layer model for real-field stratification conditions through the DJL model.

Over the resulting “breaking strip,” sediment resuspension induced by ISWs shoaling and breaking on the sloping bathymetry could play a role in the evolution of peculiar morpho-bathymetric features present in the same location. Through the Shields criterion, we give an estimation of the ISW-induced bed shear stress acting in the breaking strip area; from our calculations, we infer that ISWs shoaling and breaking could generate strong sediment resuspension in the area of contourites. Our theoretical tool for predicting ISWs breaking location may provide crucial knowledge for an ad hoc design of in situ experiments, aimed at connecting mechanistically ISWs breaking with the formation and evolution of morpho-sedimentary features.

Data Availability Statement

Bathymetric data are provided by the EMODnet–Bathymetry portal, developed in the framework of the European Marine Observation and Data Network as initiated by the European Commission (<https://www.emodnet-bathymetry.eu/>). Experimental data are publicly available at <https://doi.org/10.6084/m9.figshare.11536218.v2>.

References

- Aghsaee, P., & Boegman, L. (2015). Experimental investigation of sediment resuspension beneath internal solitary waves of depression. *Journal of Geophysical Research: Oceans*, 120(5), 3301–3314. <https://doi.org/10.1002/2014jc010401>
- Aghsaee, P., Boegman, L., Diamessis, P. J., & Lamb, K. G. (2012). Boundary-layer-separation-driven vortex shedding beneath internal solitary waves of depression. *Journal of Fluid Mechanics*, 690, 321–344.
- Aghsaee, P., Boegman, L., & Lamb, K. G. (2010). Breaking of shoaling internal solitary waves. *Journal of Fluid Mechanics*, 659, 289–317.
- Alpers, W. (1985). Theory of radar imaging of internal waves. *Nature*, 314, 245–247.
- Alpers, W., Brandt, P., & Rubino, A. (2008). Internal waves generated in the straits of Gibraltar and Messina: Observations from space. In V. Barale, & M. Gade (Eds.), *Remote Sensing of the European Seas* (pp. 319–330). Dordrecht, The Netherlands: Springer.
- Alpers, W., & Salusti, E. (1983). Scylla and Charybdis observed from space. *Journal of Geophysical Research*, 88(C3), 1800–1808.
- Alpers, W., & Vlasenko, V. (2019). Internal waves in the Andaman sea. In V. Barale, & M. Gade (Eds.), *Remote sensing in the Asian seas* (pp. 395–410). Cham, Switzerland: Springer.
- Artale, V., Levi, D., Marullo, S., & Santoleri, R. (1990). Analysis of nonlinear internal waves observed by landsat thematic mapper. *Journal of Geophysical Research*, 95(C9), 16065–16073.
- Bluteau, C., Smith, S.-L., Ivey, G., Schlosser, T., & Jones, N. (2016). *Assessing the relationship between bed shear stress estimates and observations of sediment resuspension in the ocean*. Paper presented at 20th Australasian Fluid Mechanics Conference.
- Boegman, L., & Ivey, G. N. (2009). Flow separation and resuspension beneath shoaling nonlinear internal waves. *Journal of Geophysical Research*, 114(C2). <https://doi.org/10.1029/2007jc004411>
- Boegman, L., Ivey, G., & Imberger, J. (2005). The degeneration of internal waves in lakes with sloping topography. *Limnology & Oceanography*, 50(5), 1620–1637.

Acknowledgments

This work was partially supported by EMODnet (European Marine Observation and Data Network Physics) and the Flagship Project RITMARE (The Italian Research for the Sea), coordinated by the Italian National Research Council and funded by the Italian Ministry of Education, University and Research. We thank E. Salusti for sharing his insights in the early stage of the work.

- Bourgault, D., Morsilli, M., Richards, C., Neumeier, U., & Kelley, D. E. (2014). Sediment resuspension and nepheloid layers induced by long internal solitary waves shoaling orthogonally on uniform slopes. *Continental Shelf Research*, 72, 21–33.
- Brandt, P., Rubino, A., Quadfasel, D., Alpers, W., Sellschopp, J., & Fiekas, H.-V. (1999). Evidence for the influence of Atlantic–Ionian stream fluctuations on the tidally induced internal dynamics in the Strait of Messina. *Journal of Physical Oceanography*, 29(5), 1071–1080.
- Cacchione, D. A., Pratson, L. F., & Ogston, A. S. (2002). The shaping of continental slopes by internal tides. *Science*, 296, 724–727.
- Cai, S., & Xie, J. (2010). A propagation model for the internal solitary waves in the northern South China Sea. *Journal of Geophysical Research*, 115(C12). <https://doi.org/10.1029/2010jc006341>
- Choi, W., & Camassa, R. (1999). Fully nonlinear internal waves in a two–layer fluid system. *Journal of Fluid Mechanics*, 396, 1–36.
- Dean, R., & Dalrymple, R. (1991). *Water waves mechanics for engineers and scientists*. Singapore: World Scientific.
- Dickson, R. R., & McCave, I. N. (1986). Nepheloid layers on the continental slope west of porcupine bank. *Deep Sea Research Part A. Oceanographic Research Papers*, 33(6), 791–818.
- Droghei, R., Falcini, F., Casalbore, D., Martorelli, E., Mosetti, R., Sannino, G., et al. (2016). The role of internal solitary waves on deep-water sedimentary processes: The case of up-slope migrating sediment waves off the Messina Strait. *Scientific Reports*, 6, 36376.
- Dubreil-Jacotin, M. L. (1937). Sur les theoremes d'existence relatifs aux ondes permanentes periodiques a deux dimensions dans les liquides heterogenes. *Journal de Mathematiques Pures et Appliquees*, 16, 43–67.
- Dunphy, M., Subich, C., & Stastna, M. (2011). Spectral methods for internal waves: Indistinguishable density profiles and double-humped solitary waves. *Nonlinear Processes in Geophysics*, 18, 351–358.
- Dwi Susanto, R., Mitnik, L., & Zheng, Q. (2005). Ocean internal waves observed in the Lombok Strait. *Oceanography*, 18(4), 81–87.
- Gavey, R., Carter, L., Liu, J., Talling, P. J., Hsub, R., Pope, E., et al. (2017). Frequent sediment density flows during 2006 to 2015, triggered by competing seismic and weather events: Observations from subsea cable breaks off southern Taiwan. *Marine Geology*, 384, 147–158.
- Grimshaw, R., Pelinovsky, E., Talipova, T., & Kurkin, A. (2004). Simulation of the transformation of internal solitary waves on oceanic shelves. *Journal of Physical Oceanography*, 34, 2774–2791.
- Grimshaw, R., Pelinovsky, E., Talipova, T., & Kurkina, O. (2010). Internal solitary waves: Propagation, deformation, disintegration. *Nonlinear Processes in Geophysics*, 17, 633–649.
- Helfrich, K. R. (1992). Internal solitary wave breaking and run-up on a uniform slope. *Journal of Fluid Mechanics*, 243, 133–154.
- Helfrich, K. R., & Melville, W. K. (2006). Long nonlinear waves. *Annual Review of Fluid Mechanics*, 38, 395–425.
- Jia, T., Liang, J. J., Li, X. -M., & Sha, J. (2018). SAR Observation and Numerical Simulation of Internal Solitary Wave Refraction and Reconnection Behind the Dongsha Atoll. *Journal of Geophysical Research: Oceans*, 123(1), 74–89. <https://doi.org/10.1002/2017jc013389>
- Jia, Y., Tian, Z., Shi, X., Liu, J., Chen, J., Liu, X., et al. (2019). Deep-sea sediment resuspension by internal solitary waves in the northern south China sea. *Scientific Reports*, 9, 12137.
- Kao, T. W., Pan, F.-S., & Renouard, D. (1985). Internal solitons on the pycnocline: Generation, propagation, and shoaling and breaking over a slope. *Journal of Fluid Mechanics*, 159, 19–53.
- Kodaira, T., Waseda, T., Miyata, M., & Choi, W. (2016). Internal solitary waves in a two–fluid system with a free surface. *Journal of Fluid Mechanics*, 804, 201–223.
- La Forgia, G., Adduce, C., & Falcini, F. (2018). Laboratory investigation on internal solitary waves interacting with a uniform slope. *Advances in Water Resources*, 120, 4–18.
- La Forgia, G., Adduce, C., Falcini, F., & Paola, C. (2019). Migrating Bedforms Generated by Solitary Waves. *Geophysical Research Letters*, 46(9), 4738–4746. <https://doi.org/10.1029/2019gl082511>
- La Forgia, G., Ottolenghi, L., Adduce, C., & Falcini, F. (2020). Intrusions and solitons: Propagation and collision dynamics. *Physics of Fluids*, 32(7), 076605.
- La Forgia, G., & Sciortino, G. (2019). The role of the free surface on interfacial solitary waves. *Physics of Fluids*, 31(10), 106601.
- La Forgia, G., & Sciortino, G. (2020). Interfacial solitons propagating through a background shear current. *Physics of Fluids*, 32(10), 106603.
- La Forgia, G., Tokyay, T., Adduce, C., & Constantinescu, G. (2018). Numerical investigation of breaking internal solitary waves. *Physical Review Fluids*, 3(10), 104801.
- La Forgia, G., Tokyay, T., Adduce, C., & Constantinescu, G. (2020). Bed shear stress and sediment entrainment potential for breaking of internal solitary waves. *Advances in Water Resources*, 135, 103475.
- Lamb, K. G. (2002). A numerical investigation of solitary internal waves with trapped cores formed via shoaling. *Journal of Fluid Mechanics*, 451, 109–144.
- Long, R. R. (1953). Some aspects of the flow of stratified fluids: I. A theoretical investigation. *Tellus*, 5(1), 42–58.
- Longhitano, S. (2018). Between Scylla and Charybdis (part 1): The sedimentary dynamics of the modern Messina Strait (central Mediterranean) as analogue to interpret the past. *Earth-Science Reviews*, 185, 259–287.
- Martorelli, E., Bosman, A., Casalbore, D., Chiocci, F., Conte, A. M., Di, B. L., et al. (2021). Mid-to-late Holocene upper slope contourite deposits off Capo Vaticano (Mediterranean Sea): High-resolution record of contourite cyclicity, bottom current variability and sandy facies. *Marine Geology*, 431, 106372. <https://doi.org/10.1016/j.margeo.2020.106372>
- Martorelli, E., Bosman, A., Casalbore, D., & Falcini, F. (2016). Interaction of down-slope and along-slope processes off Capo Vaticano (southern Tyrrhenian Sea, Italy), with particular reference to contourite-related landslides. *Marine Geology*, 378, 43–55.
- Marullo, S., & Santoleri, R. (1986). Fronts and internal currents at the northern mouth of the Strait of Messina. *Il Nuovo Cimento—B C*, 9(3), 701–713.
- Massel, S. (2015). *Internal gravity waves in the shallow seas*. Switzerland: Springer.
- Massel, S. (2016). On the nonlinear internal waves propagating in an inhomogeneous shallow sea. *Oceanologia*, 58, 59–70.
- Ma, X., Yan, J., Hou, Y., Lin, F., & Zheng, X. (2016). Footprints of obliquely incident internal solitary waves and internal tides near the shelf break in the northern South China Sea. *Journal of Geophysical Research: Oceans*, 121(12), 8706–8719. <https://doi.org/10.1002/2016jc012009>
- Michallet, H., & Ivey, G. (1999). Experiments on mixing due to internal solitary waves breaking on uniform slopes. *Journal of Geophysical Research*, 104(C6), 13467–13477.
- Miyata, M. (1985). An internal solitary wave of large amplitude. *LA Mer*, 23, 43–48.
- Munk, W. H., & Traylor, M. A. (1947). Refraction of Ocean Waves: A Process Linking Underwater Topography to Beach Erosion. *The Journal of Geology*, 55(1), 1–26. <https://doi.org/10.1086/625388>
- Osborne, A. R., & Burch, T. L. (1980). Internal Solitons in the Andaman Sea. *Science*, 208(4443), 451–460. <https://doi.org/10.1126/science.208.4443.451>
- Ostrovsky, L., & Stepanyants, Y. A. (1989). Do internal solitons exist in the ocean? *Reviews of Geophysics*, 27, 293–310.

- Ottolenghi, L., Adduce, C., Roman, F., & La Forgia, G. (2020). Large eddy simulations of solitons colliding with intrusions. *Physics of Fluids*, 32(9), 096606.
- Pelinovsky, E., Stepanyants, Y., & Talipova, T. (1994). Simulation of nonlinear internal wave propagation in horizontally inhomogeneous ocean. *Atmospheric and Ocean Physics*, 30, 77–83.
- Quaresma, L. S., Vitorino, J., Oliveira, A., & da Silva, J. (2007). Evidence of sediment resuspension by nonlinear internal waves on the western Portuguese mid-shelf. *Marine Geology*, 246(2), 123–143.
- Sapia, A., & Salusti, E. (1987). Observation of nonlinear internal solitary wave trains at the northern and southern mouths of the Strait of Messina. *Deep Sea Research Part A. Oceanographic Research Papers*, 34(7), 1081–1092.
- Shanmugam, G., & Wang, Y. (2015). The landslide problem. *Journal of Paleogeography*, 4(2), 109–166.
- Small, J. (2001a). A nonlinear model of the shoaling and refraction of interfacial solitary waves in the ocean. Part I: Development of the model and investigations of the shoaling effect. *Journal of Physical Oceanography*, 31(11), 3163–3183.
- Small, J. (2001b). A nonlinear model of the shoaling and refraction of interfacial solitary waves in the ocean. Part II: Oblique refraction across a continental slope and propagation over a seamount. *Journal of Physical Oceanography*, 31, 3184–3199.
- Soulsby, R. L. (1997). *Dynamics of marine sands. A manual for practical applications*, London: R. L. Soulsby and Thomas Telford Services Limited.
- Stanton, T., & Ostrovsky, L. (1998). Observations of highly nonlinear internal solitons over the Continental Shelf. *Geophysical Research Letters*, 25, 2695–2698.
- Stasna, M., & Lamb, K. G. (2002). Large fully nonlinear internal solitary waves: The effect of background current. *Physics of Fluids*, 14(9), 2987–2999.
- Sutherland, B. (2010). *Internal gravity waves*, Cambridge: Cambridge University Press.
- Sutherland, B. R., Barrett, K. J., & Ivey, G. N. (2013). Shoaling internal solitary waves. *Journal of Geophysical Research: Oceans*, 118(9), 4111–4124. <https://doi.org/10.1002/jgrc.20291>
- Turkington, B., Eydeland, A., & Wang, S. (1991). A computational method for solitary internal waves in a continuously stratified fluid. *Studies in Applied Mathematics*, 85, 93–127.
- van Rijn, L. (1993). *Principles of sediment transport in rivers, estuaries and coastal seas*. Amsterdam, The Netherlands: Aqua.
- Vercelli, E. (1925). *Il regime delle correnti e delle maree nello Stretto di Messina*. Venezia, Italy: Commissione Internazionale del Mediterraneo.
- Vlasenko, V., & Hutter, K. (2002). Numerical experiments on the breaking of solitary internal waves over a slope–shelf topography. *Journal of Physical Oceanography*, 32(6), 1779–1793.
- Vlasenko, V., & Stashchuk, N. (2007). Three-dimensional shoaling of large-amplitude internal waves. *Journal of Geophysical Research*, 112(C11), <https://doi.org/10.1029/2007jc004107>
- Xie, J., He, Z. Y., Chen, Xu, J., & Cai, S. (2015). Simulations of internal solitary wave interactions with mesoscale eddies in the Northeastern South China sea. *Journal of Physical Oceanography*, 45, 2959–2978.
- Xu, C., & Stasna, M. (2019). Internal waves in a shear background current: Transition from solitary-wave regime to dispersive-wave regime. *Physical Review Fluids*, 4, 094801.

Erratum

Due to typesetting errors, intervals of integration were reported throughout the originally published article in reverse order (i.e., the lower limit was published as the upper limit, and vice versa). These errors have been corrected, and this may be considered the official version of record.